Interpenetrating heterojunction photovoltaic cells based on C60 nano-crystallized thin films

Interpenetrating Heterojunction Photovoltaic Cells Based on C_{60} Nano-Crystallized Thin Films

Kohei Nojiri,[*a] Md. Shahiduzaman,[a] Kohei Yamamoto,[a] Takayuki Kuwabara,[a,b] Kohshin Takahashi,[a,b] and Tetsuya Taima[*a,b,c]

[a]*Graduate School of Natural Science and Technology, Kanazawa University, Kakuma, Kanazawa 920-1192, Japan*

[b]*Research Center for Sustainable Energy and Technology, Kanazawa University, Kakuma, Kanazawa 920-1192, Japan*

[c]*Institute for Frontier Science Initiative (InFIniti), Kanazawa University, Kakuma, Kanazawa, 920-1192, Japan*

* Corresponding authors: Tel: +81-76-264-6279 (T. Taima)

Fax: +81-76-264-6279 (T. Taima)

E-mail: k_nojiri@stu.kanazawa-u.ac.jp (K. Nojiri)

E-mail: taima@se.kanazawa-u.ac.jp (T. Taima)

Abstract

An interpenetrating heterojunction (IHJ) structure facilitates efficient charge separation and transport in the active layer of organic photovoltaic cells (OPVs). Additionally, the recombination of generated carriers in IHJs is reduced as these networks exhibit high carrier transport with minimal recombination sites. We have developed a simple method to fabricate nanocrystallized fullerene (C_{60}) films, which are produced by subjecting evaporated C_{60} films to either solvent spin-coating or solvent vapor annealing (SVA). The size of the rod-shaped nanocrystals in the films were controlled by changing the solvent and annealing time.

An 80-nm-diameter size nanocrystallized C_{60} film that was fabricated using SVA with ethanol was incorporated as an acceptor material in an inverted IHJ OPV cell. Tetraphenyldibenzoperiflanthene (DBP) was evaporated onto the nanocrystallized C_{60} film as the donor material. The power conversion efficiency of an IHJ OPV cell (ITO/TiOx/nanocrystallized C_{60} film/DBP/MoO_3/Au) increased from 1.79% to 2.12%, when compared with the conventional PHJ OPV cell.

KEYWORDS: *nanocrystallization, nanostructure, C_{60}, solvent treatment, organic photovoltaic cells*

Introduction

Thin-film organic photovoltaic cells (OPVs) have attracted tremendous attention for their promise to provide low cost and light weight devices that can absorb a large proportion of the solar spectrum [1-7]. OPVs commonly use either a planar heterojunction (PHJ) structure [8, 9], which consists of donor–acceptor bilayer deposition, or a bulk heterojunction (BHJ) structure, which consists of a donor–acceptor mixture as shown in Fig. 1(a) and (b), respectively. PHJ OPVs exhibit poor photocurrent density because of the limited donor–acceptor interface area. Several groups have reported that the BHJ structure increased donor–acceptor interface area by mixing the donor and acceptor materials [10, 11]. Therefore, BHJ OPVs exhibit significantly higher photocurrent densities. A drawback, caused by the mixing of materials in BHJ structures, is a low fill factor (FF). Because of space charge effects in the confines of the BHJ structure, the FF is usually lower than for a planar heterojunction [12-14]. In addition, the BHJ structure has problems of donor–acceptor phase separation and providing a continuous pathway for the dissociated charges to reach the electrode [15]. The interpenetrating heterojunction (IHJ) structure, shown in Fig. 1(c), is ideal for efficient charge separation and transport in the active layer [12, 16]. The recombination of generated carriers within IHJs is reduced because of the high carrier transport network and a lack of recombination sites between the photoactive layer and the electrodes. Both wet and dry processes are being developed to fabricate IHJ structures [12, 16-19].

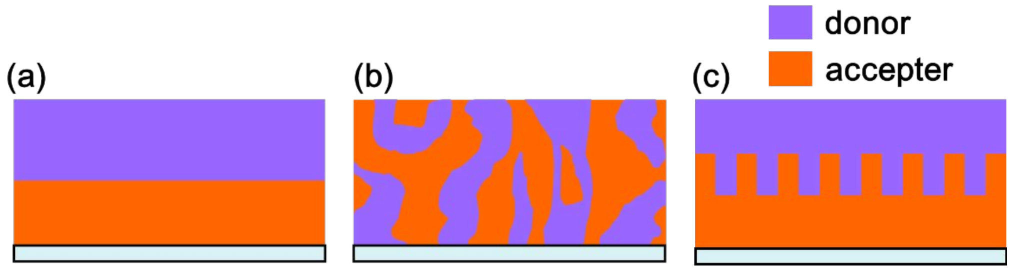

Fig. 1. Schematic illustration of (a) PHJ type structure, (b) BHJ type structure and (c) IHJ type structure.

Fujii *et al*. have reported a wet fabrication process that involves spin-coating a polymer solution onto fullerene (C_{60}) films that results in an interpenetrating structure. The solvent used to dissolve the polymer was found to dissolve the surface of the C_{60} film, which changed the surface morphology to an IHJ structure during the spin-coating process [18, 19]. Both nanoimprinting and organic vapor phase deposition are dry processes that are able to create IHJ structures [20-22]. We have previously investigated the fabrication of nanostructured organic films, focusing on three-dimensional nanopillar arrays, using glancing angle deposition (GLAD). An efficient nanostructured OPV with a power conversion efficiency (PCE) of 4.0±0.1% was fabricated by patterning a copper iodide nanorod template onto indium tin oxide (ITO) using GLAD. These approaches afforded devices with large interface areas and enhanced solar cell performances. Although these methods were successful in creating high-performing OPVs, they required special equipment for creating the nanostructures and the size and shape of the resulting structures were difficult to control [23]. M. Thomas *et al*. reported the fabrication of C_{60} nanocolumns using GLAD and revealed the superiority of IHJ structure [24].

We have developed a simple method to fabricate nanocrystallized C_{60} films by either solvent spin-coating or solvent vapor annealing (SVA) evaporated C_{60} films. We have investigated the effects of different polar solvents on the formation of the nanocrystallized C_{60} films and found that the solubility of C_{60} was important in controlling the morphology and size of the structures within the films. Nanocrystallized C_{60} films that contained structures of different sizes, created using SVA with ethanol, were used as the acceptor material in inverted IHJ OPVs.

2. Experimental Section

C_{60} (>99.9%) was purchased from Frontier Carbon Corporation. C_{60} films (60 nm) were thermally evaporated onto glass substrates in a vacuum chamber at a pressure of 5×10^{-4} Pa. Chloroform ($CHCl_3$), *n*-hexane (*n*-C_6H_{12}), and ethanol (EtOH) were used to form the nanostructures (Table 1) [25].

Table 1. Different solvents properties characteristics.

	Solubility[mg/mL]	Boiling Point[℃]	Vapor Pressure[hPa:20℃]
$CHCl_3$	0.16	61	212
n-C_6H_{14}	0.043	68	160
EtOH	0.001	78	59

The solvent spin-coating method involved 100 µl of solvent being dropped onto an evaporated C_{60} film (60 nm thick) and spin-coated at 2000 rpm for 60 sec.

The SVA method involved the C_{60} films being placed in a sealed glass container (450 ml) with a saturated solvent vapor, where 30 ml solvent was dropped in the glass container for 2 h at room temperature before C_{60} films placing.

OPVs were fabricated on ITO-patterned glass substrates that were pretreated by oxygen plasma for 20 min. Compact-TiO_x films were prepared by chemical bath deposition using the procedure described by Kuwabara *et al.* [26]. The amorphous compact TiO_x layer was deposited from an aqueous solution of titanium (IV) oxysulfate ($TiOSO_4$) and hydrogen peroxide (H_2O_2) at 80 °C for 10 min. The as-deposited TiO_x films were cleaned in an ultrasonic bath for 2 min and then heated on a hot plate at 150 °C in air for 1 h, which yielded a 30-nm-thick amorphous compact-TiO_x layer. Amorphous TiO_x films (60-nm-thick) were obtained by repeating the procedure. C_{60} films (20 nm) were then thermally evaporated on the TiO_x amorphous layer in a vacuum chamber at a pressure of 5×10^{-4} Pa. The films were then subjected to SVA using EtOH for different treatment times (0, 30, 45, and 60 min). The films were transferred to a vacuum chamber and a 40-nm-thick layer of the donor material tetraphenyldibenzoperiflanthene (DBP) was thermally evaporated onto the nanocrystallized C_{60} films at a pressure of 2×10^{-6} Pa. A hole transporting MoO_3 layer (8 nm) was thermally evaporated on top of the DBP layer. Au electrodes (80 nm) were then deposited on the MoO_3 layer at a pressure of 5×10^{-4} Pa. A schematic of the OPV cell structure (ITO/TiOx/nanocrystallized C_{60} film/DBP film/MoO_3/Au) is shown in Fig. 2(c). To determine if any remaining solvent in the films had an effect on the cells durability, nanocrystallized C_{60} films were annealed at 80 °C for 5 min on a hot plate (ND-1 (NINOS)) before depositing the DBP layer. The fabrication of the solar cells and the electrical measurements were performed at ambient temperature without exposure to air (under a vacuum or N_2 gas atmosphere). The field emission scanning electron microscopy (FE-SEM) (JSM-7610F, JEOL Ltd., JAPAN) was used to analyze the surface morphology. Surface morphology was further investigated by atomic force microscopy (AFM) (SPM-9600, Shimadzu, JAPAN). The crystallinity of the nanocrystallized C_{60} films was measured using X-ray diffractometer (XRD; Rigaku Co. SmartLab) with an X-ray tube (Cu Kα, λ = 1.5406 Å). The current density versus voltage (J-V) characteristics of the OPV cells were measured using a Keithley 2400 digital source meter when subjected to simulate AM 1.5 G solar illumination. The incident power was calibrated using a standard silicon photovoltaic system to match 1-sun intensity (100 mW/cm^2). UV-Vis absorption spectra were measured using a Hitachi U-3310 spectrophotometer.

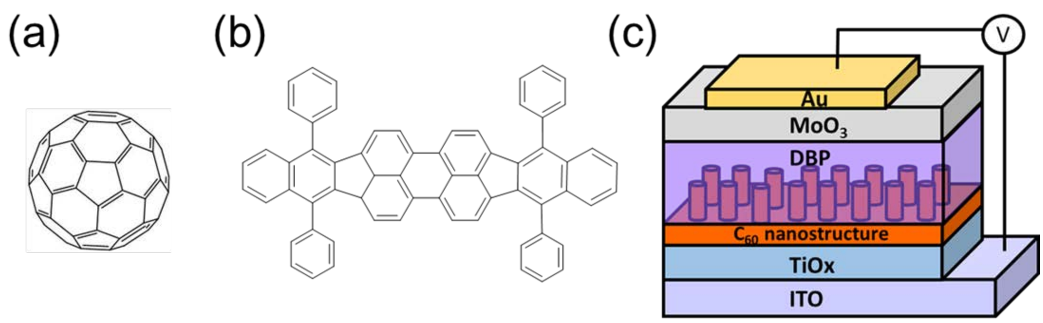

Fig. 2. Chemical structure of (a) C_{60} and (b) tetraphenyldibenzoperiflanthene (DBP) molecules. (c) Device configuration of solar cells based on C_{60} nanocrytallized.

3. Results and Discussion

SEM images of a 60-nm-thick as-deposited C_{60} film and a series of nanocrysallized films that were prepared by solvent spin-coating with $CHCl_3$, *n*-C_6H_{14}, and EtOH are shown in Fig. 3. The as-deposited C_{60} film had a smooth morphology with an average particle size of 30 nm (Fig. 3(a)). The different solvents that were used in the spin coating treatment induced different nanostructures within the films (Fig. 3(b)-(d)). C_{60} has a solubility of 0.16 mg/mL in $CHCl_3$. Treatment with this solvent induced a nanostructured film with well-developed particles between 100 and 300 nm. In contrast, the surface morphology of the films that were treated with solvents in which C_{60} has poor solubility (*n*-C_6H_{14} (0.043 mg/mL) or EtOH (0.001 mg/mL)) was almost unchanged from the as-deposited C_{60} film. Therefore, a solvent that will slightly dissolve the surface of the C_{60} thin film is required to create a nanostructured morphology. Additionally, when EtOH was used large cracks were observed in the film (Fig. 3(d)). Therefore, solvents in which C_{60} is poorly soluble such as EtOH cause damage, and peeling of the resulting thin film.

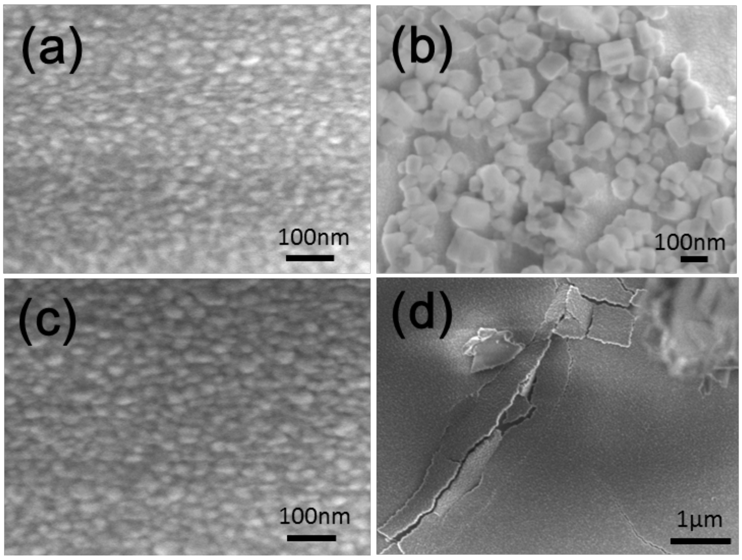

Fig. 3. SEM images of (a) a C_{60} film and C_{60} nanocrystallized films by solvent spin-coating method with (b) $CHCl_3$, (c) n-C_6H_{14}, and (d) EtOH.

This observation was further confirmed by AFM analysis. The AFM images Fig. 4(d) show the cracking morphology of the resulting film for EtOH, while the morphology was well developed for $CHCl_3$ and n-C_6H_{14}, as shown in (Figs. 4(b) and 4(c)), respectively. The as-deposited C_{60} film had smooth morphology with root-mean-square (RMS) was 2.841 nm (Fig. 4(a). The RMS roughness of the C_{60} nanocrystalized films was respectively 17.99, 1.95, and 26.85 nm at $CHCl_3$, n-C_6H_{14}, and EtOH solvent treatment by spin-coating method. The nanocrysallized film formed by solvent spin coating with $CHCl_3$ is rough (RMS: 17.99 nm) (Fig. 4(b)). Also, the surface morphology of the films that were treated with solvents in which C_{60} has poor solubility (n-C_6H_{14} or EtOH) were the same as the SEM images (Fig. 4(c) and 4(d)).

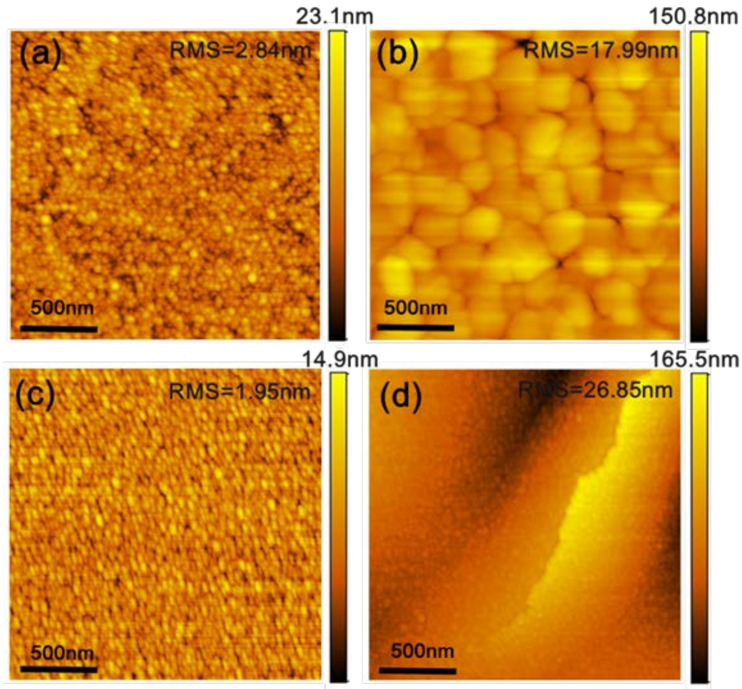

Fig. 4. AFM images of (a) a C_{60} film and C_{60} nanocrystallized films by solvent spin-coating method with (b) $CHCl_3$, (c) *n*-C_6H_{14}, and (d) EtOH.

Solvent vapor annealing (SVA) is incontestable as a cheap, simple, and precise attractive method to fabricate nanocrystallized films, which are produced by subjecting evaporated films at room temperatures. SVA is used in controlling the size of rod-shaped nanocrystals in the films by changing the solvent and annealing time. Hence, SVA techniques is used as an efficient route to fabricating nanocrystalline thin films.

SEM images of nanocrystallized C_{60} films that were prepared using SVA with $CHCl_3$, *n*-C_6H_{14}, and EtOH are shown in Fig. 5. The nanostructures that were formed by the solvents were dramatically different. A network structure that was composed of particles between 150 and 300 nm was created when $CHCl_3$ was used. In contrast to the solvent spin-coating method, when SVA was performed with either *n*-C_6H_{14} or EtOH, the resulting surface morphology was completely different from the as-prepared films. Treatment with *n*-C_6H_{14} resulted in a nanostructured film with an average particle size of approximately 500 nm. However, when EtOH was used the nanostructure changed from particles to isolated pillars, with a diameter of 150 nm. Thus, nanocrystallization occurred when the films were subjected to SVA, even when using a poor solvent for C_{60}.

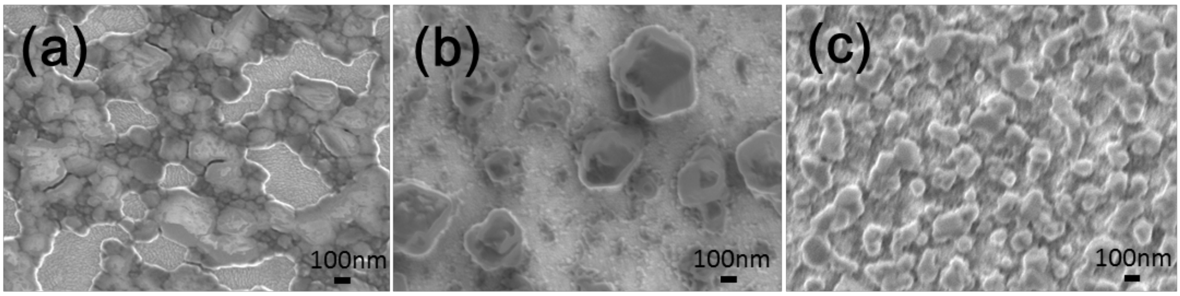

Fig. 5. SEM images of C_{60} nanocrystallized films by SVA method with (a) $CHCl_3$, (b) *n*-C_6H_{14}, and (c) EtOH.

The AFM images of Fig. 6(c) show the uniform morphology of C_{60} nanocrystallized film with EtOH, while the resulting morphology was aggregated for $CHCl_3$ and *n*-C_6H_{14} as shown in Figs. 6(a) and 6(b), respectively. The RMS roughness of the C_{60} nanocrystaline films was respectively 29.86, 103.96, and 26.02 nm at $CHCl_3$, *n*-C_6H_{14}, and EtOH. The RMS roughness was smaller with EtOH treated film than with the other solvent treatment.

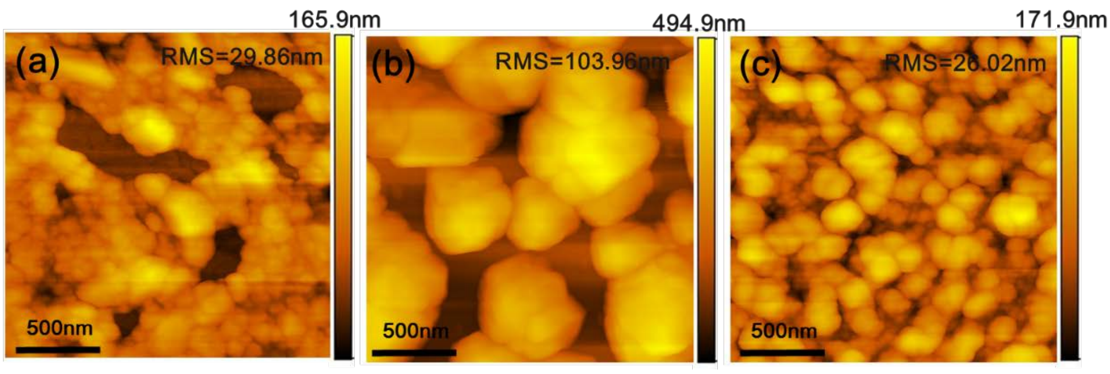

Fig. 6. AFM images of C_{60} nanocrystallized films by SVA method with (a) $CHCl_3$, (b) *n*-C_6H_{14}, and (c) EtOH.

Schematic images that illustrate the mechanisms of nanocrystallization in the C_{60} films during either solvent spin-coating or SVA are shown in Fig. 7. For nanocrystallization to occur during solvent spin-coating, the solvent must dissolve the surface of the C_{60} thin film and allow its reconstruction via self-assembly (Fig. 7(a)) [16, 17]. Following this, the substrate is rotated at 2000 rpm in order to remove the remaining solvent on the substrate and dried it for 10 min at room temperature in glove box. We spin-coated immediately dropped solvent and the total treatment time is 60 sec. When EtOH was dropped on C_{60} film surface, morphology like cracking film occurred. Due to cracking and edges, EtOH was able to pass through the C_{60} films and reach the glass substrate during the solvent soaking time. The changes that were induced in the C_{60} films during SVA were dependent upon the solubility of C_{60} in the chosen solvent. When $CHCl_3$ was used, nanocrystallization occurred via a very similar mechanism to the solvent spin-coating method. This mechanism has three steps: 1) the dissolution of the C_{60} thin film surface by the solvent vapor; 2) the reconstruction of the surface by self-assembly within the solvent vapor atmosphere; and 3) the connecting each other [27, 28]. When a poor solvent for C_{60} is used, the nanocrystallization mechanism is different. The C_{60} thin film surface is not dissolved by the solvent vapor. However, C_{60} molecules on surface can move to reduce the contact area with the solvent vapor [28, 29]. This movement causes self-assembly on the surface, which allows nanocrystallization to occur even with poor solvents (Fig. 7(b)). The treatment time for SVA was 2 h.

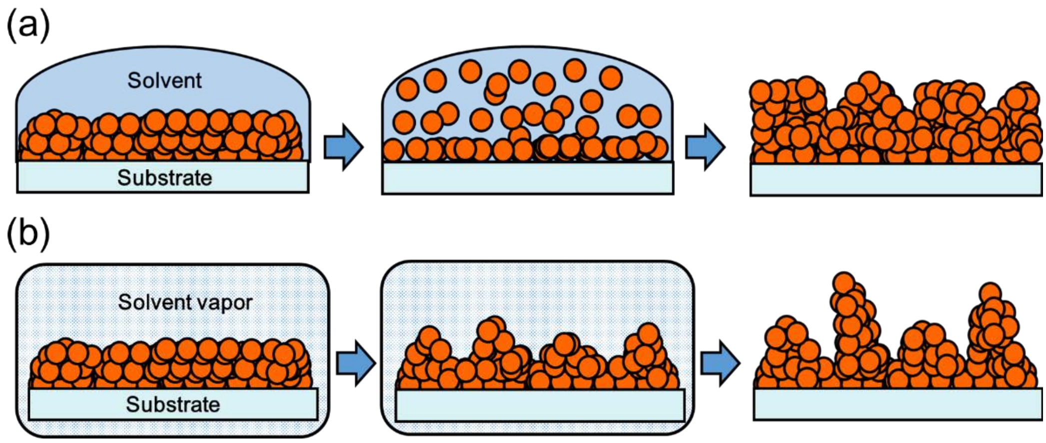

Fig. 7. Schematic illustration of formation mechanism of C_{60} nanocrystallized films by (a) spin-coating method and (b) SVA method.

XRD spectra of C_{60} films, both with and without solvent spin-coating and SVA treatments, are shown in Fig. 8. All of the films that were subjected to either solvent spin-coating or SVA exhibited large diffraction peaks at approximately $2\theta = 10.8°$, which were assigned to the (111) crystal plane [30]. This peak was not present in the spectra of the as-deposited C_{60} film. This indicated that the crystallinity of the C_{60} films improved following either solvent treatment [30]. SVA with n-C_6H_{14} gave the most intense XRD diffraction peak ($2\theta = 10.8°$), which corresponded to the film with the largest isolated nanoparticles (500 nm). Therefore, the C_{60} molecules were able to self-assemble as large and highly crystalline particles when subjected to SVA with n-C_6H_{14}. The XRD diffraction peak for the solvent spin-coating method shifted to a lower 2θ angle of 10.1°. A similar observation for a lattice expansion was reported by wang *et al.*, [31]. This lattice expansion is detrimental to the charge transport ability of a C_{60} layer in OPV applications. We also calculated mean crystalline sizes for the C_{60} treated films from the full width at half maximum of the primary peak using scherrer formula (see supporting information; Table S1). We have measured the diameter of particle size and crystalline size from SEM image and XRD spectra, respectively, as shown in Table S1.

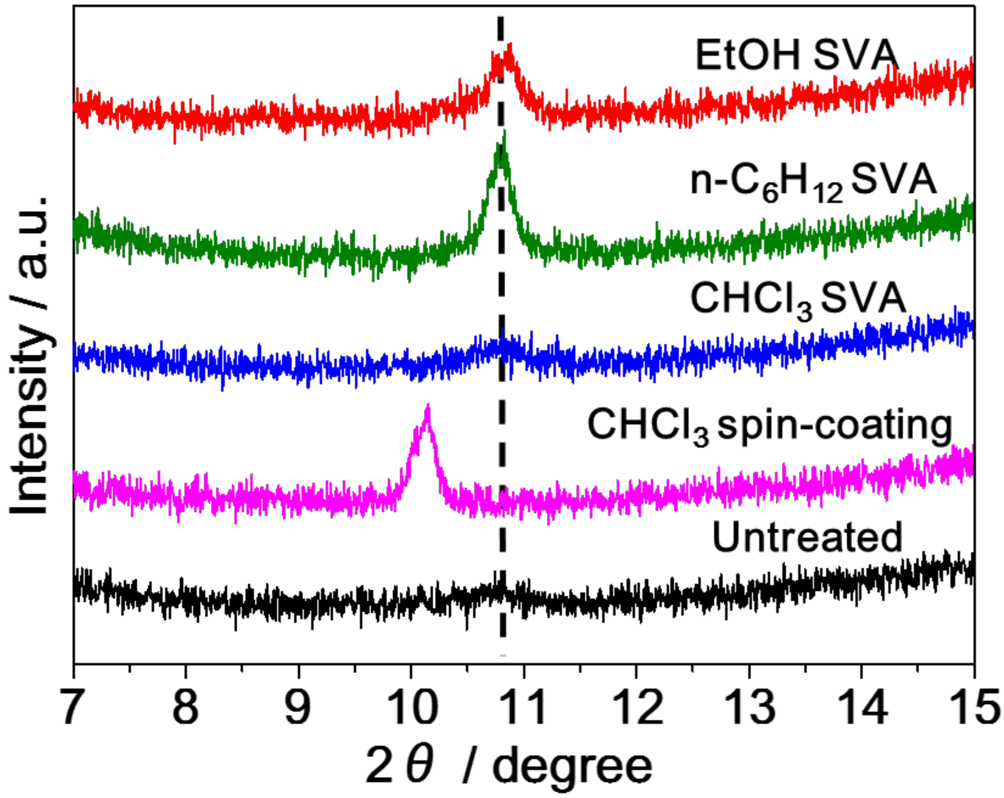

Fig. 8. XRD patterns of C_{60} films formed with and without solvent treatment.

UV-Vis spectra of C_{60} films, with or without treatment with either solvent spin-coating or SVA are shown in Fig. S1. All of the C_{60} films that were treated with solvent spin-coating or SVA exhibited an increase in absorption intensity between 300 to 500 nm compared to the untreated films. This absorption increase was caused by light scattering from the nanocrystals [32, 33], and increase crystallinity of nanocrystallized C_{60} films [34]. The UV-Vis absorption of the film subjected to SVA with n-C_6H_{14} changed significantly. This change was caused by light scattering and reflection from to the surface of the nanocrystallized film, which had become clouded. Nanocrystallized C_{60} films that contained structures of different sizes, created using SVA with EtOH, were used as the acceptor material in inverted IHJ OPVs.

Nanostructures formed by using SVA method with EtOH, which gave the ideal structure among the three solvents and leading profitable for IHJ structure as compare with solvent spin-coating method. Figures 9(a), 9(c), and 9(d) show short-circuit currents (J_{sc}), fill factor (FF), and power conversion efficiency (PCE) of the cells, respectively, in terms of SVA with EtOH in the range of different treatment times (0-60 min). J_{sc}, FF, and PCE all exhibited the same overall trend with respect to SVA with EtOH (Time/min), with maximum values treated at 30 min. The highest PCE (2.12 %), J_{sc} (3.79 mA/cm^2), and FF (0.65) were observed for the device with 30 min treated SVA containing EtOH solvent. In contrast, the open circuit voltage (V_{oc}) did not change significantly with respect to the SVA with EtOH at 30 min treated solar cells, as shown in Fig. 9(b).

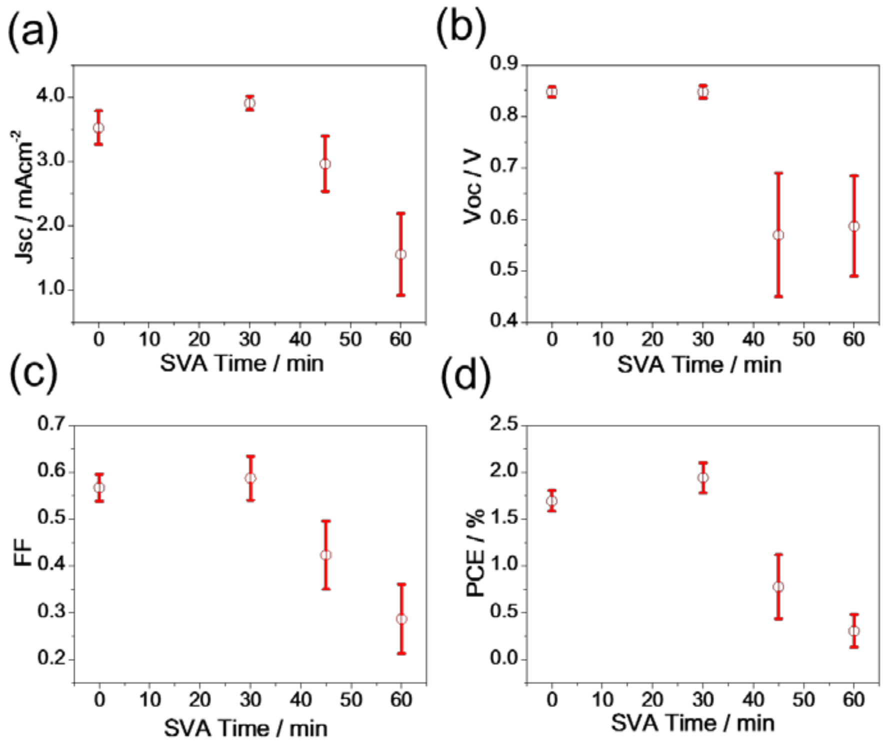

Fig. 9. Characteristics of C_{60} nanocrystallized based solar cells as a function of the SVA treated with EtOH (Time/min): (a) short-circuit current density, J_{sc}, (b) open-circuit voltage, V_{oc}, (c) fill factor, FF, and (d) power conversion efficiency, PCE. Error bars show plus-or-minus one standard deviation from the mean.

We further compares the device characteristics of the IHJ C_{60} nanocrystallied films based solar cells by showing *J*-*V* curves measured for cells with different treatment times in Fig. 10. Nanocrystallized films that were subjected to SVA with EtOH for different treatment times (0, 30, 45, and 60 min) were incorporated into inverted IHJ OPVs and SEM images of each films are shown in Fig. S2. An amorphous, evaporated DBP layer was used as both a donor layer and a means to form a smooth surface on top of the nanocrystallized C_{60} film. The device structure consisted of ITO/TiOx/nanocrystallized C_{60} film (20nm)/DBP film (40 nm)/MoO_3/Au, as shown in Fig. 1. The solar cell parameters are listed in Table 2. The OPV that contained the nanocrystallized C_{60} film that was treated for 30 min exhibited higher solar cell performance compared with the cell that contained the untreated (0 min) C_{60} layer (PHJ OPV). The particle diameter size of C_{60} films in the IHJ OPV cell were approximately 80 nm, while those within the PHJ cell were 30 nm. The difference in the size of the particles resulted in a larger donor-acceptor interface area (10% increment), as determined from analysis using AFM (Fig. S3). Both the J_{sc} and the FFs improved from 3.46 to 3.79 mA/cm^2 and 0.60 to 0.65, respectively. This increase in donor-acceptor interface area was consistent with the 10% improvement that was observed in the J_{sc}. Therefore, the higher J_{sc} of IHJ OPV (30-min treatment) was caused by increased interface area [22, 23], while the higher FF was caused by increased charge transport ability within the nanocrystallized C_{60} films [27]. To produce high-performance IHJ OPVs, controllable morphology and crystallinity is very important. The better morphology together with control size and shape of C_{60} layer treated with 30 min sample can collect electrons more efficiently at the interface of donor-acceptor, thus preventing to a large leakage current and recombination of charge carriers. The series resistance is decreased from 21.7 to 18.2 Ω/cm^2, whereas the shunt resistance is increased from 2737.8 to 3188.6 Ω/cm^2 upon the untreated (0 min) and treated (30 min) of C_{60} layers based devices, respectively. This result indicates that the nanocrystallized C_{60} film enhanced charge carrier extraction from photoactive layer to electrode, and improving the *Jsc* and nanocrystallized C_{60} film decreased the leakage current. Besides, crystallinity of C_{60} film also increased. The enhanced crystallization improved the charge transport ability, hence FF was improved. Therefore, the IHJ OPV (30-min treatment) exhibited an improved PCE of 2.1% when compared with the PHJ OPV (0-min treatment, PCE = 1.8%). The solar cell performance of the IHJ OPVs that contained nanocrystallized C_{60} films that were treated for 45 and 60 min decreased non homogeneous morphology. The particle diameter size of within these films was 160 nm and 180 nm, respectively. These large particles diameter sizes produced rough films that caused high current-leakage, which resulted in low FF and V_{oc} values.

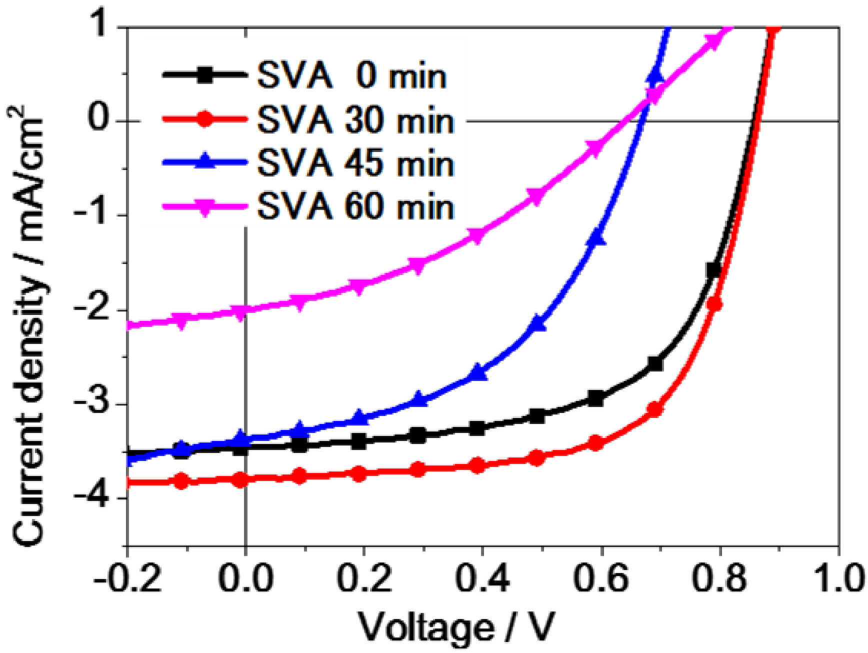

Fig. 10. *J-V* characteristics obtained for the solar cells based on C_{60} nanocrystallized thin films.

Table 2. Average value with standard deviation and highest value of cell performance characteristics of ITO/Compact-TiOx/80 nm-size C_{60} nanocrystallized film/DBP/MoO_3/Au IHJ type OPV, respectively.

SVA Time	J_{sc} [mA/cm^2]	V_{oc} [V]	FF	PCE (%)
0min	3.52±0.26(3.46)	0.85±0.01(0.86)	0.57±0.03(0.60)	1.69±0.11(1.79)

30min	3.90±0.11(3.79)	0.85±0.01(0.86)	0.59±0.04(0.65)	1.94±0.16(2.12)
45min	2.96±0.44(3.37)	0.57±0.12(0.67)	0.42±0.07(0.48)	0.78±0.34(1.08)
60min	1.56±0.64(2.01)	0.59±0.10(0.64)	0.29±0.07(0.37)	0.31±0.18(0.47)

The durability of the IHJ OPVs that contained the interpenetrating nanocrystallized C_{60} films treated for 30 min was tested under a N_2 atmosphere (Fig. 11). Due to light soaking effect, PCE was improved after 5 min, which is confirmed by the inclusion of the references from co-author Kuwabara, *et al.* [35, 36]. The PCE of the PHJ OPV (0-min treatment) remained almost unchanged following irradiation with light for 2 h. However, the PCE of the IHJ OPV (30-min treatment) decreased to 70% of the maximum value after light irradiation for 2 h. This decrease was not observed in the IHJ OPV (30-min treatment) that contained the C_{60} layer that was annealed at 80 °C (5 min) after SVA. As the annealing temperature is higher than the boiling point of EtOH, this result suggested that solvent remained in the nanocrystallized C_{60} film, which led to the observed decrease of the cell durability. Importantly, the interpenetrating structure exhibited the same durability as the PHJ when the solvent was removed by thermal annealing. Thus, when solvent annealing processes like SVA are used, any solvent that remains in the organic thin film may significantly affect the cells performance and durability, so removing the solvent completely is necessary.

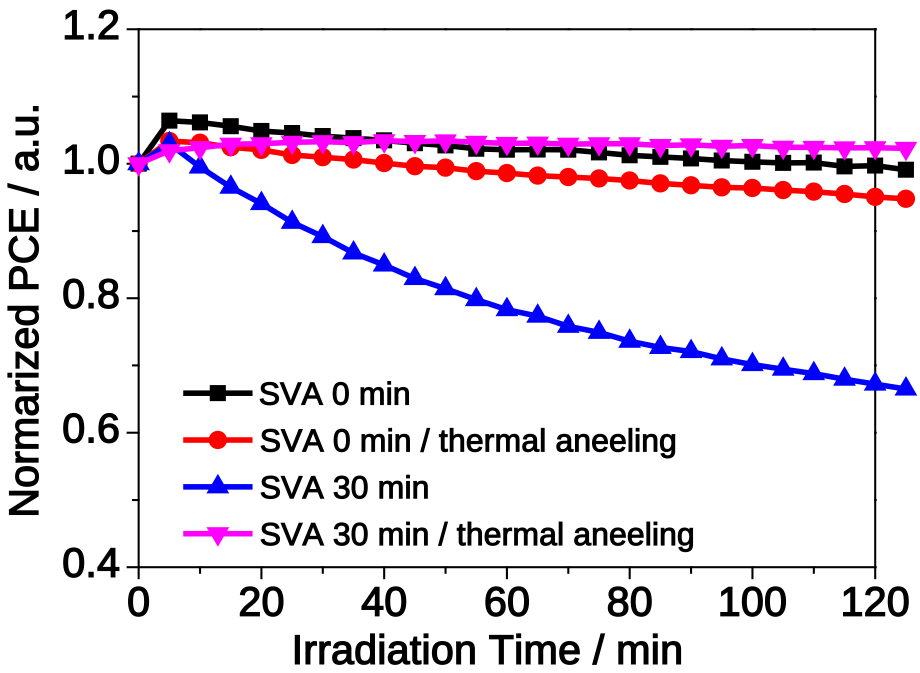

Fig. 11. Durability curves of the normalized PCE.

4. Conclusions

We have demonstrated a method to fabricate nanocrystallized C_{60} films with different structures using both solvent spin-coating and SVA. The crystalline structures of the films and the mechanisms of their formation were investigated. These were then incorporated into OPV cells and studied. For nanocrystallization to occur during the solvent spin-coating method, a solvent in which C_{60} is partially soluble is required. In contrast, when using the SVA method, nanocrystallization occurs when using a poor solvent for C_{60}. When EtOH was used an ideal IHJ structure was formed. Thus, SVA requires a poor solvent for C_{60} and long treatment times to create nanocrystallized films with the appropriate sized rod-shape particles for OPV applications. A IHJ OPV cell that contained controllable morphology together with 80-nm-particle diameter size nanocrystallized C_{60} film, fabricated using SVA with EtOH, exhibited a higher J_{sc} value than the PHJ OPV cell that contained untreated C_{60} films. This was caused by an increase in interface area, while the higher FF observed was caused by the increased charge transport ability within the nanocrystallized C_{60} film. The nanocrystallization of C_{60} caused improved crystallinity, which had a significant influence on the charge transport ability of a C_{60} layer. As a result, the PCE improved from 1.8% to 2.1% when compared with the conventional PHJ OPV cell. The durability of the OPV cells that contained a C_{60} layer subjected to SVA with EtOH improved when the C_{60} layer was thermally annealed. This improvement occurred because the remaining solvent in the nanocrystallized C_{60} film was removed. We have shown that nanocrystallized films, formed by solvent treatment, can lead to IHJ structured OPV cells with significant improvements over a PHJ structure. Fabrication of nanocrystallized film using a solvent treatment can be expected to further applications and higher performance of OPV cells.

Acknowledgement

This work was supported by the Incorporated Administrative Agency New Energy and Industrial Technology Development Organization (NEDO) under the Ministry of Economy, Trade and Industry (METI).

References

[1] Y. Zhou, T. Taima, T. Miyadera, T. Yamanari, M. Kitamura, K. Nakatsu and Y. Yoshida, Glancing Angle Deposition of Copper Iodide Nanocrystals for Efficient Organic Photovoltaics, *Nano Lett.* 12 (2012) 4146-4152.

[2] G. Li, R. Zhu, and Y. Yang, Nat. Photon. 6 (2012) 153-161.

[3] S. Günes, H. Neugebauer, and N. S. Sariciftci, Chem. Rev. 107 (2007) 1324–1338.
[4] N. S. Lewis, Science 315 (2007) 798-801.
[5] L. Yang, T. Zhang, H. Zhou, S. C. Price, B. J. Wiley, and W. You, ACS Appl. Mater. Interfaces 3 (2011) 4075-4084.
[6] K. Cheng, M.-H. Yang, W. W. W. Chiu, C.-Y. Huang, J. Chang, T.-F. Ying, and Y. Yang, Macromol. Rapid Commun. 26 (2005) 247-264.
[7] K.-H. Choi, J.-A. Jeong, J.-W. Kang, D.-G. Kim, J. K. Kim, S.-I. Na, D.-Y. Kim, S.-S. Kim, and H.-K. Kim, Sol. Energy Mater. Sol. Cells 93 (2009) 1248-1255.
[8] Z. He, C. Zhong, S. Su, M. Xu, H. Wu, and Y. Cao, Nat. Photonics 6 (2012) 591-595.
[9] J.C. Wang, X.C. Ren, S.Q. Shi, C.W. Leung, Paddy K. L. Chan, Org. Electron. 12 (2011) 880–885.
[10] C. J. Brabec, S. Gowrisanker, J. J. M. Halls, D. Laird, S. Jia, and S. P. Williams, Adv. Mater. 22 (2010) 3839-3856.
[11] M. C. Scharber, D. Mühlbacher, M. Koppe, P. Denk, C. Waldauf, A. J. Heeger, and C. J. Brabec, Adv. Mater. 18 (2006) 789-794.
[12] F. Yang, M. Shtein, Stephen R. Forrest, Nature Mater. 4 (2005) 37-41.
[13] G. Yu, J. Gao, J. C. Hummelen, F. Wudi, A. J. Heeger, Science, 270 (1995) 1789-1791.
[14] P. Peumans, S. Uchida, S. R. Forrest, Nature 425 (2003) 158–162.
[15] S.R. Forrest, MRS Bull. 30 (2005) 28-32.
[16] Y. Zheng, R. Bekele, J. Ouyang, J. Xue, Org. Electron. 10 (2009) 1621–1625.
[17] J. G. Van Dijken, M. D. Fleischauer, M. J. Brett, J. Mater. Chem. 21 (2011) 1013-1019.
[18] A. Fujii, T. Shirakawa, T. Umeda, H. Mizukami, Y. Hashimoto, K. Yoshino, Jpn. J. Appl. Phys. 43 (2004) 5573-5576.
[19] T. Umeda, Y. Hashimoto H. Mizukami, A. Fujii, K. Yoshino, Jpn. J. Appl. Phys. 44 (2005) 4155-4160.
[20] M. Aryal, K. Trivedi, W. (Walter) Hu, ACS Nano 3 (2009) 3085–3090.
[21] S. Jeong, C. Cho, H. Kang, K-H. Kim, Y. Yuk, J. Young Park, Bumjoon J. Kim, J-Y. Lee, ACS Nano 9 (2015) 2773–2782.
[22] Y. Zhou, T. Taima, T. Kuwabara, K. Takahashi, Adv. Mater. 25 (2013) 6069–6075.
[23] Y. Zhou, T. Taima, T. Miyadera, T. Yamanari, M. Kitamura, K. Nakatsu, Y. Yoshida, Nano Lett. 12 (2012) 4146–4152.
[24] M. Thomas, B. J. Worfolk, D. A. Rider, M. T. Taschuk, J. M. Buriak, M. J. Brett, ACS Appl. Mater. Interfaces, 3 (2011) 1887–1894.
[25] R. S. Ruoff, D. S. Tse, R. Malhotra, D. C. Lorents, J. Phys. Chem. 97 (1993) 3379-3383
[26] T. Kuwabara, H. Sugiyama, M. Kuzuba, T. Yamaguchi and K. Takahashi, Org. Electron. 11 (2010) 1136–1140.
[27] M. Li, F. Liu, X. Wan, W. Ni, B. Kan, H. Feng, Q. Zhang, X. Yang, Y. Wang, Y. Zhang, Y. Shen, T. P. Russell, Y. Chen, Adv. Mater. 27 (2015) 6296–6302.

[28] Y. Zheng, S. Li, D. Zheng, J. Yu, Org. Electron. 15 (2014) 2647–2653.
[29] S. Nam, D. S. Chung, J. Jang, S. H. Kim, C. Yang, S.-K. Kwon, C. E. Park, Journal of The Electrochemical Society 157 (2010) 90-93.
[30] L. Wang, B. Liu, D. Liu, M. Yao, Y. Hou, S. Yu, T. Cui, D. Li, G. Zou, A. Iwasiewicz, B. Sundqvist, Adv. Mater. 18 (2006) 1883–1888.
[31] L. Wang, B. Liu, D. Liu, M. Yao, S. Yu, Y. Hou, B. Zou, T. Cui, G. Zou, Appl. Phys. Lett. 91 (2007) 103112-1-3.
[32] T. P. Chou, Q. Zhang, G. E. Fryxell, G. Cao, Adv. Mater. 19 (2007) 2588–2592.
[33] Q. Zhang, C. S. Dandeneau, X. Zhou, G Cao, Adv. Mater. 21 (2009) 4087–4108.
[34] Y. Zhou, T. Taima, T. Miyadera, T. Yamanari, M. Kitamura, K. Nakatsu, Y. Yoshida, Appl. Phys. Lett. 100 (2012) 233302-1-5.
[35] T. Kuwabara, C. Iwata, T. Yamaguchi, K Takahashi, ACS Appl. Mater. Interfaces, 2 (2010) 2254–2260.
[36] T. Kuwabara, K. Yano, T. Yamaguchi, T. Taima, K. Takahashi, D. Son, K. Marumoto, J. Phys. Chem. 119 (2015) 5274−5280.